Integrating tide-driven wetland soil redox and biogeochemical interactions into a land surface model

Benjamin N. Sulman[1], Jiaze Wang[1,2], Sophie LaFond-Hudson[1,3], Teri O'Meara[1], Fengming Yuan[1], Sergi Molins[4], Glenn Hammond[5], Inke Forbrich[6,7], Zoe Cardon[7], and Anne Giblin[7]

1. Environmental Sciences Division and Climate Change Science Institute, Oak Ridge National Laboratory, Oak Ridge, TN.
2. School of Earth and Climate Sciences, University of Maine, Orono, ME.
3. Upper Midwest Water Science Center, U.S. Geological Survey, Madison, WI.
4. Earth and Environmental Sciences Division, Lawrence Berkeley National Laboratory, Berkeley, CA.
5. Environmental Subsurface Science Group, Pacific Northwest National Laboratory, Richland, WA.
6. Department of Environmental Sciences, University of Toledo, Toledo, OH.
7. The Ecosystems Center, Marine Biological Laboratory, Woods Hole, MA.

Corresponding author: Benjamin Sulman (sulmanbn@ornl.gov)

Key points:

- Coastal wetlands store large amounts of carbon and are sensitive to chemical interactions driven by salinity and tidal fluctuations
- We coupled a land surface model to a reactive transport model to simulate biogeochemical cycling in saline and fresh tidal wetlands
- Sulfate availability in saline wetlands lowered simulated methane emissions, which compared well with site measurements

Abstract

Redox processes, aqueous and solid-phase chemistry, and pH dynamics are key drivers of subsurface biogeochemical cycling in terrestrial and wetland ecosystems but are typically not included in terrestrial carbon cycle models. These omissions may introduce errors when simulating systems where redox interactions and pH fluctuations are important, such as wetlands where saturation of soils can produce anoxic conditions and coastal systems where sulfate inputs from seawater can influence biogeochemistry. Integrating cycling of redox-sensitive elements could therefore allow models to better represent key elements of carbon cycling and greenhouse gas production. We describe a model framework that couples the Energy Exascale Earth System Model (E3SM) Land Model (ELM) with PFLOTRAN biogeochemistry, allowing geochemical processes and redox interactions to be integrated with land surface model simulations. We implemented a reaction network including aerobic decomposition, fermentation, sulfate reduction, sulfide oxidation, and methanogenesis as well as pH dynamics along with iron oxide and iron sulfide mineral precipitation and dissolution. We simulated biogeochemical cycling in tidal wetlands subject to either saltwater or freshwater inputs driven by tidal hydrological dynamics. In simulations with saltwater tidal inputs, sulfate reduction led to accumulation of sulfide, higher dissolved inorganic carbon concentrations, lower dissolved organic carbon concentrations, and lower methane emissions than simulations with freshwater tidal inputs. Model simulations compared well with measured porewater concentrations and surface gas emissions from coastal wetlands in the Northeastern United States. These results demonstrate how simulating geochemical reaction networks can improve land surface model simulations of subsurface biogeochemistry and carbon cycling.

Plain language summary:

Coastal wetlands can store carbon rapidly but are difficult to represent in current models for accurate accounting of how much carbon can be trapped. This difficulty is due to the complex interactions between tides, chemical reactions, and water salinity, which strongly affect the decay of organic matter and the production of greenhouse gases. We enhanced an existing model by linking it to a powerful chemical reaction simulator such that organic matter decomposition was tightly connected to chemical reactions involving key components such as sulfur, iron, oxygen, and methane. We used this model to compute the effect of salinity on organic matter decomposition and greenhouse gas production in saline and freshwater wetlands. The model predicted much lower methane emissions from saltwater-affected wetlands, which compared well to field measurements from coastal wetland sites in Massachusetts, USA. This model improves the accounting of carbon in wetland ecosystems and opens a broad range of possibilities for representing complex chemistry in land models.

1 Introduction

Coastal wetlands can sequester carbon at exceptionally high rates (McLeod et al., 2011), and emissions of greenhouse gases such as methane are highly sensitive to salinity, and particularly to sulfur cycling driven by seawater influence in coastal systems (Poffenbarger et al., 2011). Changes in sulfur dynamics and seawater influence can also contribute to peat collapse and rapid carbon loss in coastal wetland systems subject to changing sea levels (Chambers et al., 2019). Tidal wetlands represent a key challenge for existing carbon cycle modeling frameworks, due to

their outsized role in the carbon cycling and the complex combination of hydrology, redox dynamics, and interactions of different chemical cycles that drive subsurface biogeochemistry in these systems (Ward et al., 2020).

Chemical interactions including pH dynamics, redox cycling, oxygen consumption, and mineral interactions are recognized as key drivers of soil carbon cycling in both oxic (Hall et al., 2018; Li et al., 2021; Sollins et al., 1996) and anoxic (Kögel-Knabner et al., 2010; Lipson et al., 2010; Sutton-Grier et al., 2011) environments. Redox interactions are particularly important in determining greenhouse gas emissions in inundated soils subject to redox fluctuations (Ginn et al., 2017; B. N. Sulman et al., 2022). However, land surface models (LSMs) that are used to simulate and project carbon and nutrient cycling as part of Earth system model (ESM) simulations typically use simplified representations of organic matter cycling that include only carbon, macronutrients (N and P), water, and energy cycling (Todd-Brown et al., 2013). These omissions could drive uncertainties and predictive errors when simulating biogeochemical responses to changing hydrological conditions or projecting carbon cycling across different soil types.

In saturated soils, the omission of redox cycling and oxygen concentrations could lead to bias in simulations of organic matter degradation as well as greenhouse gas production. Existing LSMs typically treat soil saturation as a proxy for redox state, assuming that saturated conditions translate directly to oxygen depletion (Wania et al., 2013). In reality, both organic matter decomposition and methane (CH_4) production are sensitive to the presence and depletion of terminal electron acceptors (TEAs) including oxygen, iron, sulfate, nitrate, and manganese (Estop-Aragonés et al., 2013; Herndon et al., 2015; Poffenbarger et al., 2011). While some models do include a temporal delay in methane (CH_4) production as a proxy for the depletion of TEAs (Riley et al., 2011), such proxy approaches may not be sufficient to represent variations in TEA patterns across variations in soil mineral content or in situations where flows of dissolved oxygen or plant-mediated oxygen transport are important. In frequently flooded coastal or riparian systems, such approaches may not adequately represent the addition and mixing of TEAs, and may fail to accurately predict methane fluxes in coastal systems where increasing sulfate availability suppresses methane production even as water levels rise (Kirwan et al., 2023). Redox conditions and porewater chemical concentrations can also affect plant growth. For example, plant tolerance to salinity and inundation varies widely (LaFond-Hudson & Sulman, 2023) and sulfides produced via sulfate reduction under anoxic conditions can be toxic to plants (Koch et al., 1990; Lamers et al., 2013). Thus, representing dynamics of redox-active chemical species may allow LSMs to simulate wetland carbon cycling processes and greenhouse gas emissions more accurately.

Incorporating representation of chemical interactions directly into LSM codes has been challenging due to the complexity of introducing processes specific to individual chemicals into already-complex model structures. Specialized reactive transport simulators do exist that can simulate complex biogeochemical reaction networks (Frei et al., 2012; G. E. Hammond et al., 2014; Perzan et al., 2021; Steefel et al., 2015; J. Tang et al., 2022), and simulators such as PFLOTRAN (G. E. Hammond et al., 2014) include flexible configuration systems allowing alternative reaction network structures to be represented without work-intensive changes to model code (Glenn E. Hammond, 2022). Previous work to couple reactive transport simulators to existing LSMs has demonstrated the feasibility of offloading biogeochemical calculations from fixed representations in LSM code to more flexible reaction network simulators, but these implementations have not previously moved beyond demonstrating that existing LSM soil C and

macronutrient representations can be reproduced in the coupled codes (G. Tang et al., 2016; J. Tang et al., 2022).

Here, we present a method that couples the Energy Exascale Earth System Model (E3SM) Land Model (ELM; Burrows et al., 2020) to the reaction network simulator PFLOTRAN (G. E. Hammond et al., 2014) via the application programming interface (API) Alquimia (Andre et al., 2013) to enable simulations of flexibly defined reaction networks and robust representation of oxygen and TEA concentrations, mineral precipitation and dissolution, and chemical interactions with organic matter cycling within an LSM. As a demonstration of the model framework, we simulate the effect of tidal cycling on subsurface oxygen and salinity concentrations as well as sulfur cycling in tidal wetland soils, and we compare simulated production and surface emissions of carbon dioxide and methane across gradients of salinity.

2 Methods

2.1 Biogeochemical reaction network

We implemented a network of reactions including soil organic matter (SOM) decomposition and aqueous redox chemistry in PFLOTRAN (G. E. Hammond et al., 2014), building on a previous PFLOTRAN implementation of redox biogeochemistry applied to Arctic soils (B. N. Sulman et al., 2022). SOM decomposition reactions were implemented in the PFLOTRAN Reaction Sandbox (Hammond, 2022) using the same decomposition kinetics used in ELM SOM and litter decomposition calculations (G. Tang et al., 2016). ELM litter and SOM decomposition follows pseudo-first-order kinetics with nutrient limitation according to a "converging trophic cascade" (CTC) framework (Burrows et al., 2020; P. E. Thornton et al., 2002) (Fig. 1, upper right). Litter and coarse woody debris (CWD) pools decompose into SOM pools with fixed decomposition time scales (modified by temperature and moisture) and fixed C:N ratios. N mineralization or immobilization is determined by the relative C:N ratio of successive pools and the fraction of the pool C that is converted to CO_2 during a decomposition transition. Organic matter pools decompose as a solid-state process, transforming from one solid organic matter pool to the next with associated production of mineralized N and CO_2. While ELM can simulate phosphorus (P) as well as N cycling (Yang et al., 2014), the current PFLOTRAN framework for decomposition omits P. Inorganic N pools (NO^{3-} and NH^{4+}) are also tracked, accounting for N mineralization and immobilization as well as plant root N uptake. Root N uptake rates are calculated based on plant N demand and a Michaelis-Menten function of inorganic N availability.

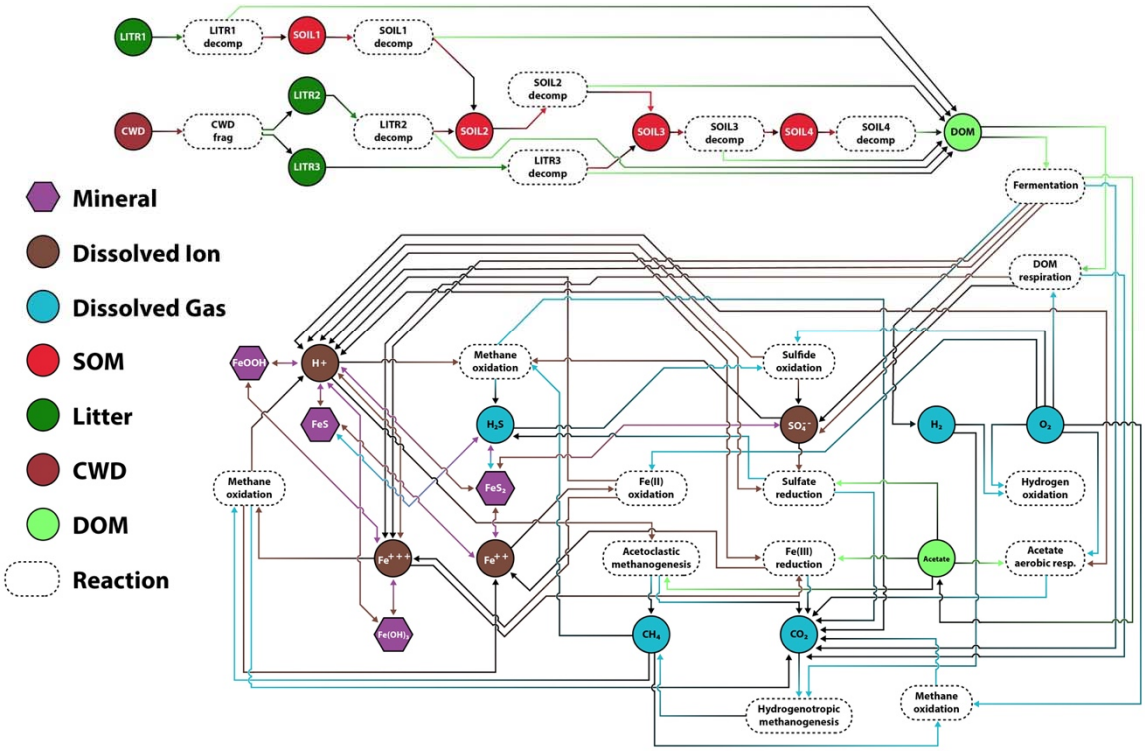

Figure 1: Diagram of the biogeochemical reaction network used in the simulations. Pools are shown as circles, color coded by type of pool (including coarse woody debris [CWD], soil organic matter [SOM], and dissolved organic matter [DOM] along with dissolved gases and ions). Arrows indicate transformations via the reactions shown in white ovals. Note that multiple methane oxidation pathways involving oxygen, sulfate, and iron are shown as separate reactions. Nitrogen pools and related reactions are omitted from the diagram for clarity.

To incorporate dissolved oxygen consumption and aqueous-phase redox reactions into the reaction network (Table 1; Fig. 1, lower portion), decomposition of litter and SOM pools was modified so that the decomposed fraction previously converted directly to CO_2 was converted instead to DOM with a fixed C:N ratio of 20. Multiple aqueous-phase chemical reactions were added representing alternative pathways of DOM decomposition, with liberated N, Fe, and sulfate content of organic matter included based on fixed stoichiometry of DOM (C:N:S:Fe = 2000:100:20:1), based on measurements of C, S, and Fe content *Spartina alterniflora* litter from Massachusetts sites (Breteler et al., 1981) and a global synthesis showing a median plant litter Fe concentration of 0.2 g kg^{-1} (Peng et al., 2023). In addition to aerobic decomposition of DOM, which consumes oxygen, anaerobic reactions including fermentation, iron reduction, sulfate reduction, and methanogenesis are included in the reaction network. Methane oxidation by oxygen, iron, or sulfate is also included. Following previous applications of this framework (B. N. Sulman et al., 2022), redox reactions are implemented as multi-Monod type reactions that could include both substrate and inhibition interactions:

$$R = V_{max}(T) \prod_N \frac{C_{S_N}}{K_{S_N}+C_{S_N}} \prod_M \frac{K_{I_M}}{K_{I_M}+C_{I_M}} \quad (1)$$

where R is reaction rate (mol (L H_2O)$^{-1}$ s^{-1}), V_{max} is temperature-dependent maximum reaction rate (mol L^{-1} s^{-1}), N is the set of reactant species (including substrates and terminal electron acceptors), M is the set of inhibiting species, C_{S_N} is the concentration of the Nth substrate, K_{S_N} is the half-saturation constant of the Nth substrate, C_{I_M} is the concentration of the Mth inhibiting species, and K_{I_M} is the inhibition constant of the Mth inhibiting species. Reaction stoichiometries, rates, half-saturations, and inhibition species are shown in Table 1. Inhibition is used to prevent anaerobic reactions from occurring in oxic soil layers, and to represent the dependence of fermentation on pH and buildup of acetate concentrations. The reaction network does not include direct inhibition of redox reactions by the presence of alternative electron acceptors (e.g., inhibition of iron reduction by sulfate or inhibition of methanogenesis by Fe^{+++}), apart from oxygen. Rate constants and half-reaction parameters built on values used for the earlier implementation of the reaction network (B. N. Sulman et al., 2022) or used literature values where available, as specified in Table 1. Values for parameters that could not be directly constrained using literature data were estimated based on rates relative to similar reactions in the network.

All aqueous reactions have a reaction rate modified by temperature sensitivity via an Arrhenius relationship:

$$V_{max}(T) = V_0 e^{\frac{Ea}{R}(\frac{1}{298.15}-\frac{1}{T+273.15})} \quad (2)$$

Where V_0 is the maximum reaction rate at reference temperature, Ea is activation energy, R is the ideal gas constant (8.314 J mol^{-1}), and T is temperature in C. Ea was set to 80 kJ mol^{-1} (approximately a Q10 of 3.0 at 20ºC) for sulfate reduction and methanogenesis, and 50 kJ mol^{-1} (approximately a Q10 of 2.0 at 20ºC) for other reactions reflecting the higher temperature sensitivity of methanogenesis and sulfate reduction relative to aerobic respiration (Inglett et al., 2012).

PFLOTRAN solves for the mass balance of each component according to the stoichiometric relationships defined by all reactions, including kinetic (Table 1) and equilibrium reactions. pH is tracked dynamically from the appropriate proton balance of aqueous-phase biogeochemical reactions and mineral precipitation/dissolution, incorporating aqueous speciation as part of the solution, e.g. CO_2/HCO_3^- and H_2S/HS^- partitioning. The biogeochemical conceptual model incorporates key aqueous complexation (e.g., carbonates, sulfides, etc.) and mineral precipitation-dissolution (pyrite, Fe oxides, etc.) reactions that buffer the system with respect to pH. Fermentation has a net acidifying effect due to proton release, as do sulfide oxidation and pyrite dissolution. Fe(III) reduction causes a net increase in pH, because it is coupled to proton-absorbing dissolution of Fe oxide minerals.

Table 1: Biogeochemical reactions and parameters included in the reaction network.

Reaction name	**Stoichiometry**	**Rate constant (mol L H_2O^{-1} s^{-1})**	**Monod half saturations (mol L H_2O^{-1})**	**Inhibition half saturations (mol L H_2O^{-1})**	**Parameter source**
DOM aerobic	DOM + $O_2 \rightarrow CO_2$ + 0.05 NH_4^++	2x10^{-6}	DOM (0.1)		(B. N.

decomposition	0.01 SO_4^{2-} + 0.005 Fe^{3+}		O_2 ($1x10^{-4}$)		Sulman et al., 2022)
Fermentation	DOM + 1/3 H_2O → 1/3 CH_3COO^- + 1/3 CO_2 + 1/3 H^+ + 2/3 H_2 + 0.05 NH^{4+} + 0.01 SO_4^{2-} + 0.005 Fe^{3+}	$1.5x10^{-6}$	DOM (0.1)	O_2 ($1x10^{-4}$) CH_3COO^- (0.02) H^+ ($1x10^{-4}$)	Sulman et al. 2022
Acetate aerobic respiration	CH_3COO^- + 2 O_2 + H^+ → 2 CO_2 + 2 H_2O	$3x10^{-6}$	O_2 ($1x10^{-4}$) CH_3COO^- (0.04)		Sulman et al. 2022
Hydrogen oxidation	2 H_2 + O_2 → 2 H_2O	$2x10^{-6}$	H_2 (0.1) O_2 ($1x10^{-4}$)		Assumed similar rate to other oxidation reactions
Sulfate reduction	CH_3COO^- + SO_4^{2-} + 2 H^+ → 2 CO_2 + HS^-	$1x10^{-8}$	CH_3COO^- (0.04) SO_4^{2-} ($1x10^{-4}$) H^+ ($1x10^{-6}$)	O_2 ($1x10^{-4}$)	(Iversen & Jorgensen, 1985)
Sulfide oxidation	HS^- + 2 O_2 → SO_4^{2-} + H^+	$1x10^{-7}$	O_2 ($1x10^{-4}$) HS^- ($1x10^{-4}$)		Assumed an order of magnitude slower than H_2 and acetate oxidation
Fe(III) reduction	CH_3COO^- + 8 Fe^{3+} + 2 H_2O → 2 CO_2 + 8 Fe^{2+} + 7 H^+	$2.25x10^{-8}$	CH_3COO^- (0.04) Fe^{3+} ($1x10^{-9}$)	O_2 ($1x10^{-4}$)	Sulman et al. 2022
Fe(II) oxidation	Fe^{2+} + 0.25 O_2 + H^+ → Fe^{3+} + 0.5 H_2O	$1x10^{-6}$	O_2 ($1x10^{-4}$) Fe^{2+} (0.1) H^+ ($1x10^{-5}$)		Sulman et al. 2022
Acetoclastic methanogenesis	CH_3COO^- + H^+ → CH_4 + CO_2	$1.5x10^{-8}$	CH_3COO^- (0.04) H^+ ($1x10^{-5.54}$)	O_2 ($1x10^{-5}$) H^+ ($1x10^{-5.54}$)	Sulman et al. 2022
Hydrogenotrophic methanogenesis	4 H_2 + CO_2 → CH_4 + 2 H_2O	$9.6x10^{-9}$	H_2 (0.1) CO_2 (0.1)	O_2 ($1x10^{-5}$)	Sulman et al., 2022
Methane oxidation (O_2)	CH_4 + 2 O_2 → CO_2 + 2 H_2O	$4x10^{-8}$	O_2 ($1x10^{-4}$) CH_4 ($1x10^{-3}$)		(King et al., 1990)
Methane oxidation (sulfate)	CH_4 + SO_4^{2-} + H^+ → CO_2 + HS^- + 2 H_2O	$3x10^{-10}$	SO_4^{2-} ($1x10^{-4}$) CH_4 ($1x10^{-3}$)		(Iversen & Jorgensen, 1985)
Methane oxidation (Fe)	CH_4 + 8 Fe^{3+} + 2 H_2O → CO_2 + 8 Fe^{2+} + 8 H^+	$3x10^{-10}$	Fe^{3+} ($8x10^{-9}$) CH4 ($1x10^{-3}$)		Assumed similar rate to sulfate-mediated oxidation
$Fe(OH)_3$	$Fe(OH)_3$ + 3 H^+ ↔ Fe^{3+} + 3 H_2O	$1x10^{-10}$			
Goethite	FeOOH + 3 H^+ ↔ Fe^{3+} + 2 H_2O	$1x10^{-13}$			
Pyrite	FeS_2 + H_2O ↔ 0.25 H^+ + 0.25 SO_4^{2-} + Fe^{2+} + 1.75 HS^-	$1x10^{-13}$			

Pyrrhotite	$FeS + H^+ \leftrightarrow Fe^{2+} + HS^-$	$1x10^{-11}$			

2.2 Coupling via the Alquimia interface

PFLOTRAN is coupled to ELM via the Alquimia interface (Andre et al., 2013), which is designed as a standardized application programming interface (API) for incorporating existing third-party biogeochemistry codes within environmental transport models. Alquimia has previously been used to connect the Advanced Terrestrial Simulator (ATS) model with PFLOTRAN for watershed-scale reactive transport simulations (Jan et al., 2021; Molins et al., 2022; Xu et al., 2022). Alquimia organizes key chemical information into mobile and immobile (sorbed) concentrations of solutes, as well as volumetric fractions of minerals. The API also includes functions for initialization, equilibration of initial and boundary conditions, and time stepping the geochemical model. Here, we implemented the Alquimia API within ELM. Alquimia initialization and initial condition equilibration subroutines were added to the ELM initialization code, and the Alquimia time stepping subroutine was added to the ELM code as described below. PFLOTRAN input and database files are read as part of the initialization process to specify the chemical species, reaction network, and reaction parameters such as rate constants, inhibition factors and thermodynamic equilibrium constants.

ELM represents key carbon and nitrogen pools including multiple litter and SOM pools as well as soil nitrate and ammonium. These pools are all represented in the PFLOTRAN reaction network used in these simulations, building on previous work to represent ELM decomposition processes in PFLOTRAN (G. Tang et al., 2016). We modified the Alquimia interface to treat solid-state SOM pools as immobile chemicals within the Alquimia data structure, allowing transparent data transfer of SOM pools from ELM to PFLOTRAN and back via the interface. This structure allows the ELM decomposition processes to be fully replaced by equivalent or modified calculations on the PFLOTRAN side, updating C and N concentrations and maintaining C and N mass balance while enabling interactions with reaction networks of arbitrary complexity as determined by the PFLOTRAN input file, provided that all ELM SOM C and N pools are included in the PFLOTRAN reaction network.

Coupling within the ELM-PFLOTRAN framework is modular, with ELM storing the state variables (e.g., concentrations) while PFLOTRAN calculates chemical transformations. However, only data that are directly relevant to ELM state (primarily organic matter and nutrient pools) are translated into ELM data structures that are visible to other model components. This allows representation of different reaction networks to have minimal effects on other parts of ELM code, and allows simulation of different reaction network configurations and complexities without any changes to ELM code specific to a particular reaction network configuration.

2.3 Vertical gas and solute transport

ELM-PFLOTRAN employs operator splitting for reactive transport: ELM simulates the 1D gas and solute transport within vertical columns and calls PFLOTRAN (through Alquimia) to solve the 0D biogeochemistry for each layer in the 1D column. Vertical advection-diffusion is implemented using the finite volume approach of (Patankar, 1980). The current gas diffusion implementation does not divide soluble gases into dissolved and gas phases, but instead treats them as solutes with a higher diffusion rate in unsaturated soil layers. Diffusion coefficients are set separately for gas and non-gas solutes. Gas diffusion coefficient decreases with increasing water saturation based on (Fan et al., 2014):

$$D_g = 1.3x10^{-5}(\theta_{sat} - \theta)\left(1 - \frac{\theta}{\theta_{sat}}\right)^3 \quad (3)$$

where D_g is gas diffusion coefficient (m^2/s), θ is soil volumetric water content (m^3/m^3), and θ_{sat} is soil volumetric water content at saturation (i.e., porosity). Diffusion coefficient of aqueous solutes is based on (Wright, n.d.):

$$D_a = 1.25x10^{-11}e^{10*\theta} \quad (4)$$

where D_a is aqueous diffusion coefficient ($m^2\ s^{-1}$). At the beginning of the column calculation, gas concentrations in the top layer are assumed to be in equilibrium with the upper boundary layer concentrations if the top layer is unsaturated. Vertical advection of solutes is calculated by assuming that vertical flow downward from each layer is equal to the subsurface drainage flow rate of the column as calculated by ELM. Solute concentrations in downward vertical flows into the top layer are determined by the upper boundary condition. Vertical flow out of the bottom of the deepest soil layer is assumed to be zero.

Ebullition is included as a transport pathway for dissolved gases. Pressure in each layer is calculated using the weight of water in layers above, including atmospheric pressure. Partial pressure of each dissolved gas is calculated based on a temperature-dependent Henry's law relationship with a gas-specific Henry's Law constant (see Table 2):

$$P_g = \frac{C_g}{H_g e^{-H_{T,g}(\frac{1}{T} - \frac{1}{298.15})}} \quad (5)$$

Where P_g is partial pressure of gas g, C_g is concentration of gas g (mol m^{-3}), H_g is the Henry's Law constant for gas g (mol m^{-3} Pa^{-1}), and $H_{T,g}$ is the temperature dependence of solubility for gas g (K^{-1}). If partial pressure of a dissolved gas exceeded the ambient pressure, the excess concentration is removed from the layer, reducing the gas concentration in the lower layer to the saturation value. 90% of the excess is moved upward one layer, thus assuming that bubbles can be re-dissolved in unsaturated upper layers. The remaining 10% is emitted to the atmosphere, representing a fraction of bubbles that move more rapidly to the surface. This process is conducted starting in the bottom layer and moving up the profile.

Table 2: Henry's Law constants and temperature dependence coefficients for dissolved gases in the model.

Dissolved gas	Henry's Law constant (mol m^{-3} Pa^{-1})	Temperature dependence (K^{-1})
CO_2	$3.3x10^{-4}$	2400
CH_4	$1.4x10^{-5}$	1900
O_2	$1.2x10^{-5}$	1700
H_2S	$1.0x10^{-3}$	2100
H_2	$7.7x10^{-6}$	530

2.4 Time stepping approach

Vertical transport and chemical reactions are calculated with an operator splitting approach using Strang splitting (Strang, 1968) to reduce truncation error related to operator splitting (Carrayrou et al., 2004). A variable time stepping approach is used to account for failure of the chemical reaction simulator to converge to a valid solution when the simulated time step is too long compared to the time scale of chemical reactions, or when consumption of gases (e.g., O_2) is high enough that transport calculations at that time step will underestimate gas concentrations. One half time step of vertical transport is calculated first, and gas concentrations in the surface soil layer are equilibrated with the upper boundary condition. Next, chemistry is updated via Alquimia/PFLOTRAN for each soil layer, starting at the top. If any soil layer fails to converge to a valid solution, then concentrations in all layers are reset and the time step is cut in half. When the top layer is unsaturated, a reduction of greater than 25% in dissolved oxygen concentration in the top layer (which is assumed to be near equilibrium with the atmosphere) is also treated as a nonconvergence condition, because it indicates that the current time step length cannot accurately capture the rate of oxygen consumption and/or transport in the column. The column reactive transport calculations, and potential shortening of the time step, are repeated recursively until chemistry in all layers can be successfully updated. Then, the second half time step of vertical transport is calculated. The shortened time steps are repeated appropriately to ensure that the total integration matches the ELM time step (60 minutes in our simulations) because ELM does not natively support flexible time stepping.

2.5 Tidal forcing

Lateral flows into and out of the soil column built on previous work focused on boreal peatland microtopography (Shi et al., 2015) and initial implementation of tides in coastal systems that used hydrologically coupled soil columns and a sinusoidal tidal pattern (O'Meara et al., 2021). Lateral flows and tidal-driven exchange of water and solutes in this approach use a hydrological boundary condition determined by the relative height of water in a tidal channel compared with water table height in the wetland soil column. We extended the previous lateral flow implementation, which used a single lateral flow time scale, to include rapid horizontal flow when the water table or tidal water level was above the soil surface to equilibrate the surface water depth in the wetland to the tide height.

$$Q_{surf} = (z_{tide} - z_{surf})\, k_{surf} \quad (6)$$

Where Q_{surf} is horizontal surface water flow into the wetland column (mm s^{-1}), z_{tide} is height of water in the tidal channel (mm, relative to wetland soil surface height), z_{surf} is surface water height in the wetland (mm, defined as zero when water table is below the surface), and k_{surf} is a rate constant representing the time scale of surface water transfer as a function of the difference in surface water height, set to a rapid flow to so that surface water level is close to equilibrium with the tidal forcing (7×10^{-5} s^{-1}). Consistent with the previous lateral flow implementation, a slower drainage flux allows water to flow into or out of the soil column during low tide conditions when the water table and tide height are below the surface:

$$Q_{subsurf} = (z_{tide} - z_{WT})\, k_{subsurf} \quad (7)$$

Where $Q_{subsurf}$ is horizontal net subsurface water flow into the wetland column, z_{WT} is water table depth in the wetland subsurface (defined as < 0), and $k_{subsurf}$ is the rate constant for subsurface net flow, calculated using the mean saturated hydraulic conductivity of the column (Shi et al., 2015). In addition, ELM calculates a subsurface drainage flow rate as a function of water table depth:

$$Q_{drain} = 2x10^{-3}(1 - f_{ice})e^{0.4\, z_{WT}} \quad (8)$$

Where Q_{drain} is net subsurface drainage rate and f_{ice} is an increasing function of mean column ice fraction (accounting for decreased drainage through frozen layers).

Horizontal flows in ELM (including Q_{surf}, $Q_{subsurf}$, and Q_{drain}) are currently calculated using a "bucket" approach that is not fully integrated with vertical flow. Vertical flows are calculated first, according to a Richards Equation approach. Next, total horizontal water outflow during the time step is removed from the column by subtracting water content from each layer one at a time, moving downward starting from the water table. Conversely, water flowing into the column is added to the layer above the water table until it reaches saturation, with the process repeated moving upwards by layer until the appropriate total amount of water has been added to the column. Because horizontal flows were not fully integrated into the ELM calculations for vertical flow within the column, the combined hydrology did not yield reasonable results for solute transport. Therefore, we represented vertical transport of solutes assuming that vertical flows balanced subsurface drainage:

$$\begin{cases} Q_{vert}(z) = Q_{drain}, \ z < z_{max} \\ Q_{vert}(z) = 0, \ z = z_{max} \end{cases} \quad (9)$$

Where Q_{vert} is vertical flow out of the layer, z is layer depth, and z_{max} is depth of the bottommost layer.

Lateral inflow as well as infiltration during flooded conditions are assumed to have the solute concentrations of the tidal boundary condition, which is supplied as salinity concentration in an external forcing dataset. Sulfate concentration is assumed to equal 14% of the concentration of chloride (on a per mass basis). pH is calculated using a linear approximation of pH = 6.0 for fresh water and pH = 8.0 for saltwater with a salinity of 30 ppt.

Because comprehensive concentration data for all compounds in the reaction network were not available for the tidal boundary condition, salinity and sulfate are exchanged horizontally via tidal flows while other solutes (including nitrogen) are assumed to stay primarily in the soil column. Specifically, when calculating vertical and lateral transport 10% of the mass of solutes without a defined freshwater/saltwater boundary condition (that is, excluding pH, salinity, and sulfate) was available for transport and leaching while the remaining 90% remained in the soil layer. This estimated soluble fraction approach was necessary to prevent excessive leaching of nutrients out of the subsurface. Excessive nitrogen leaking could potentially be addressed by incorporating sorption of ammonium on soil surfaces into the reaction network.

2.6 ELM simulations

Simulations used a standard ELM spinup process (Peter E. Thornton & Rosenbloom, 2005) of 50 years of accelerated decomposition spinup followed by 100 years of regular spinup and 150

years of transient (historical) simulation. Atmospheric forcing, including temperature and precipitation, used downscaled Global Soil Wetness Project Phase 3 (GSWP3) meteorology for the Plum Island Ecosystems site, repeated as necessary for spinup. Tidal forcing used sinusoidal tide constituents available from NOAA Tides and Currents for the Plum Island low marsh site (Station ID 8441241), with reference height corrected so that tidal height was defined relative to the marsh surface.

To test the role of salinity and associated S cycling on biogeochemistry and greenhouse gas fluxes in the model, we compared three model configurations for simulating the low marsh ecosystem. All models included the same tidal hydrology patterns. In the Fresh configuration, salinity in tide water was set to zero. In the Saline configuration, salinity in the tide water use measured concentrations from the tidal forcing dataset, which ranged from 24 to 35 ppt. In the Saline + reduced GPP configuration, the same saline tide water concentrations were used, and gross primary production (GPP) was additionally reduced as a function of tidal salinity level to represent the impact of saline conditions on plant productivity:

$$f(s) = e^{\frac{-(s-\mu)^2}{2\Lambda^2}} \quad (10)$$

Where f(s) is the salinity effect on root water uptake resistance (varying between 0 and 1), s is tidewater salinity (ppt), μ is the optimal salinity (-22 ppt), and Λ is the salinity tolerance (30 ppt), based on observed salinity responses of *Spartina alterniflora* (LaFond-Hudson & Sulman, 2023; Vasquez et al., 2006). This parameterization yielded a 40-50% reduction in mean daily GPP when salinity was taken into account.

2.7 Comparison with measurements

Model simulations of geochemical processes were evaluated by comparing simulated profiles of salinity, sulfide, and DOC concentrations to measurements from the low marsh sites through the PIE LTER monitoring program (Giblin et al., 2021). Specifically, salinity and sulfide measurements from the Law's Point site are shown in Figures 2d and 4f (squares), and DOC and sulfide measurements from the Shad Creek site at 4 m from the creek edge are shown in Figures 4f (circles) and 4i, measured monthly in May-October 2017, are shown in Figures 2 and 4 in comparison to model simulations. In addition, simulated surface fluxes are compared with eddy covariance flux measurements of carbon dioxide and methane from the PIE LTER low marsh flux tower site (Giblin & Forbrich, 2022) (Ameriflux site US-PLM). Hydrological patterns were compared with measured water levels at the site (Giblin, 2021). The site is a low marsh dominated by *Spartina alterniflora* within the Shad Creek catchment in Rowley, MA. Simulated soil organic matter concentration profiles are compared with measured profiles from PIE LTER marsh sites (Spivak, 2020). Uncertainty ranges in measured SOM profiles were calculated using the standard error of the mean over three replicate profiles.

3 Results

3.1 Simulated hydrology

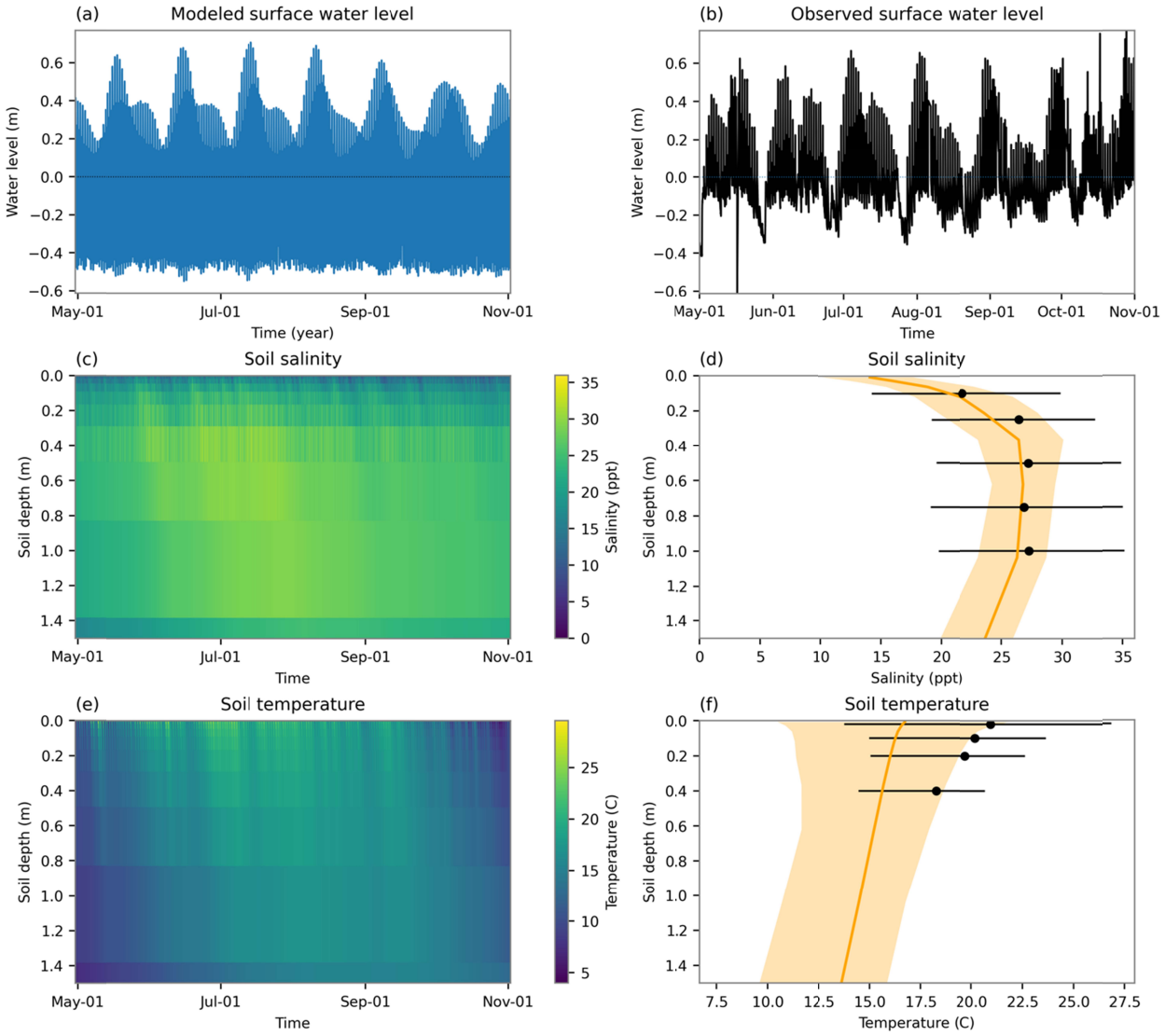

Figure 2: Water levels, soil salinity, and soil temperature over May-November. Profile plots (panels d and f) show the time-averaged profile (solid line) and the 10th and 90th percentile values (shaded region). Black circles and error bars in panels d and f show observations with 10%-90% percentile ranges.

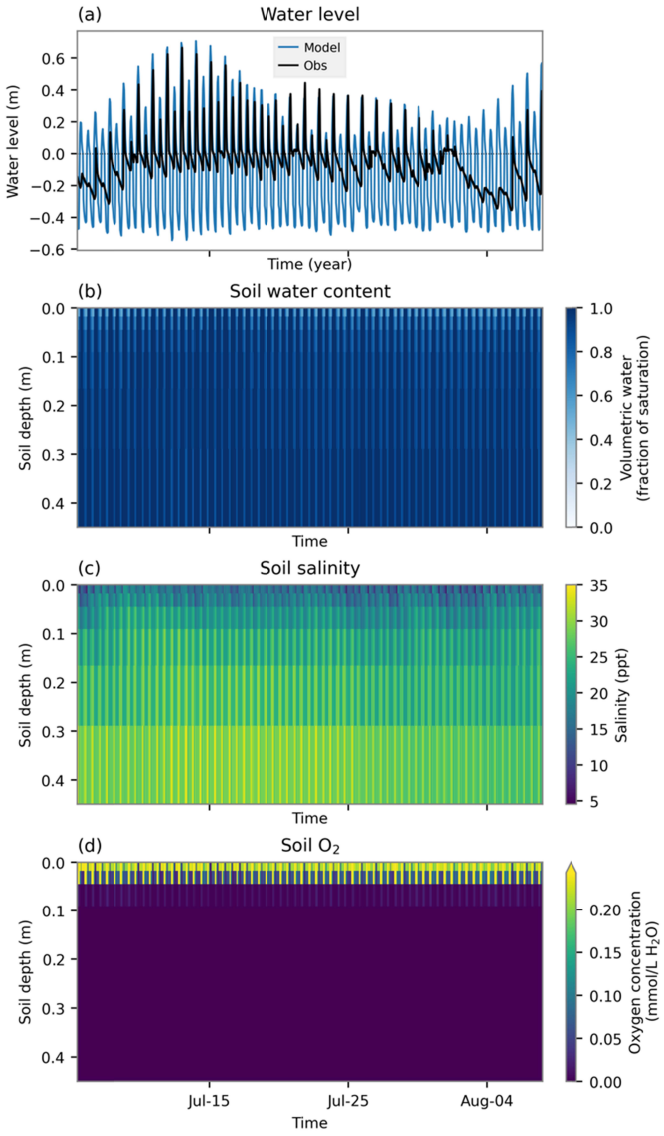

Figure 3: Simulated surface water depth (a), volumetric water content (b), salinity (c), and oxygen concentration (d) over an approximately one month time period. Observed water level is also shown as a black line in panel (a). Observed water levels were shifted by 9 days to account for a temporal mismatch in tide timing between model forcing and observations.

The tidal-driven hydrological model, paired with a time series of hourly tide height and salinity, allowed the model to simulate patterns of surface water depth across diel tidal fluctuations as well as longer-term variations in tide height (e.g., spring/neap tide cycles; Fig. 2a, 3a). The study site represents a low marsh, where the water table generally stays close to the surface even during low-tide conditions (Fig. 2b). Simulations showed unsaturated soil conditions in the top 50 cm of the soil profile during low tides (Fig. 2a, 3b), while observed water table during low tides generally stayed within 5-10 cm of the surface. However, the deeper unsaturated layers in the model remained quite wet (> 75% of saturation below 5 cm), limiting oxygen concentrations below 5-10 cm depth (Fig. 3d). The tidal inundation cycle was visible in soil oxygen concentrations, with oxygen in the subsurface depleted rapidly during flooded periods.

Salinity increased with depth in the top 50 cm and varied with tidal fluctuations, reflecting the influence of salinity inputs at the soil surface and transport into the subsurface, combined with the solute concentrating effect of water removal from the root zone driven by transpiration (Fig. 2c, 3c). Simulated salinity matched well with the observed range for the low marsh site (Fig. 2d). Simulated subsurface temperatures at the site ranged from below freezing during winter to 20ºC during summer (Fig. 2e,f), with the greatest range of temperatures occurring near the surface. Simulated soil temperatures were about 5ºC lower than the observed range.

3.2 Simulated redox and sulfur cycling

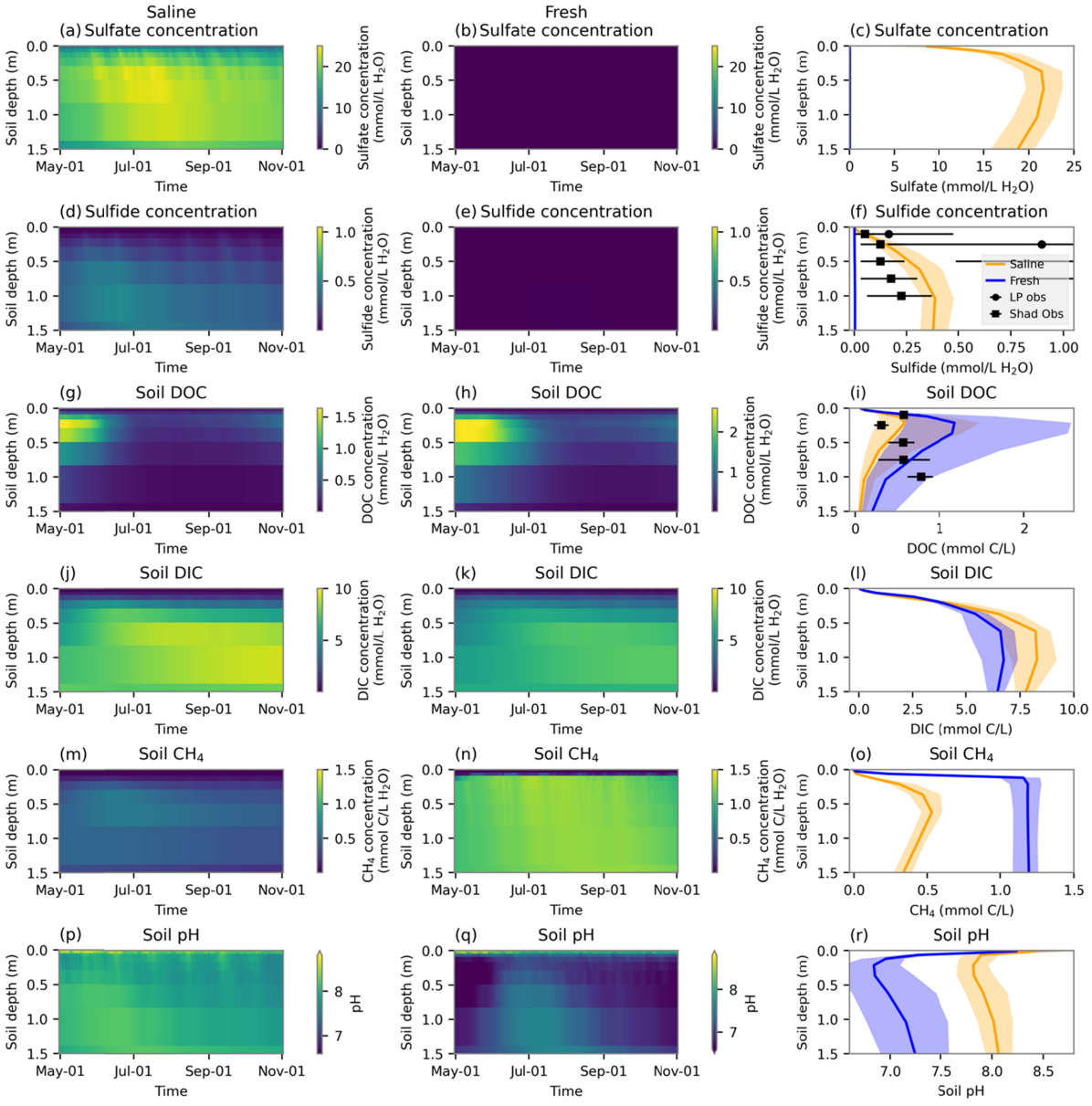

Figure 4: Simulated biogeochemistry over a growing season. The left column shows profiles over time for the saline simulation, and the middle column shows profiles over time for the freshwater

simulation. The right column shows mean profiles (solid lines) for the saline (orange) and fresh (blue) simulation, respectively. Shaded regions show the 10^{th} to 90^{th} percentile range of values. Black symbols in (f) and (i) show measured values. Squares in (f) show sulfide measurements from the Shad Creek site (4 m from the creek bank) and circles show measurements from the Law's Point (LP) site.

The reaction network in the model connected carbon, sulfur, and oxygen cycling in the subsurface (Fig. 1) and responded to seasonal and tidal cycles. Sulfate concentration in water entering the soil profile through infiltration or lateral flows was assumed to be proportional to salinity, leading to sulfate profiles that qualitatively resembled salinity profiles, both peaking at about 30 cm depth (Fig. 4a,c; 2c,d). Sulfate reduction produced sulfide in anoxic layers, driving a sulfide concentration profile that peaked at a deeper 80-100 cm depth (Fig. 4d,f). Simulated sulfide concentrations were within the lower range of observed values, with observed profiles ranging from 0.1 to 4 mM and simulated profiles in the saline configuration ranging up to 0.3 mM. Sulfate concentrations were much lower in the freshwater configuration than in the saline configuration, driving differences in subsurface biogeochemistry (Fig. 4b,e). Sulfate reduction consumed DOC, lowering DOC concentrations in layers below 10 cm depth in saline relative to fresh simulations (Fig. 4i). DOC concentrations increased in spring and peaked at a depth of about 30 cm. Simulated DOC concentrations in the saline simulation were within the range of measured concentrations (0.1 – 1 mM), although the peeper measurement technique may underestimate DOC concentrations (A. Giblin, personal communication). DOC was rapidly depleted in summer as sulfate reduction and methanogenesis rates increased. DIC concentrations (including dissolved CO_2 and CH_4; Fig 4j-l) increased at the same time of year as DIC was produced by both sulfate reduction and methanogenesis. Subsurface methane concentrations (Fig. 4m-o) also increased as DOC was depleted. pH was lower in the freshwater simulations than in the saline simulation, and declined as DIC concentrations increased (Fig. 4p-r).

Methane concentrations were low near the surface and increased in deeper layers, reflecting the predominance of methane production in more reducing subsurface layers and the consumption of methane in more oxidizing layers. Along with oxygen and Fe(III), sulfate also served as a substrate for methane oxidation, which lowered subsurface methane concentrations in the saline simulation compared to the fresh simulation. Peak methane efflux was 20 times higher in the fresh simulation than in the saline simulation (Fig. 5a), with a seasonal cycle increasing rapidly in spring and continuing through the fall. The very low methane fluxes from the saline simulation were consistent with the magnitude of fluxes measured from the low marsh flux tower (Fig. 5b). Surface methane flux lagged methane production, as methane produced in deep layers was initially oxidized in upper layers until more shallow layers of the profile reached saturation later in the warm season. Saline simulations in which vegetation productivity was also reduced had 40-50% lower surface methane emissions and were closer in magnitude to observed fluxes than saline simulations without reduced vegetation productivity.

Soil CO_2 fluxes (excluding autotrophic root respiration) were slightly higher for the saline simulation than for the fresh simulation (Fig. 5c). CO_2 fluxes from the reduced GPP simulation were 25-50% lower than for the saline simulation without reductions in GPP, indicating the impact of reduced C inputs to the system. Simulated loss of DIC through lateral tidal flows were about one fourth the magnitude of surface CO_2 efflux, and represented a greater total carbon flux than methane emissions (Fig. 5d).

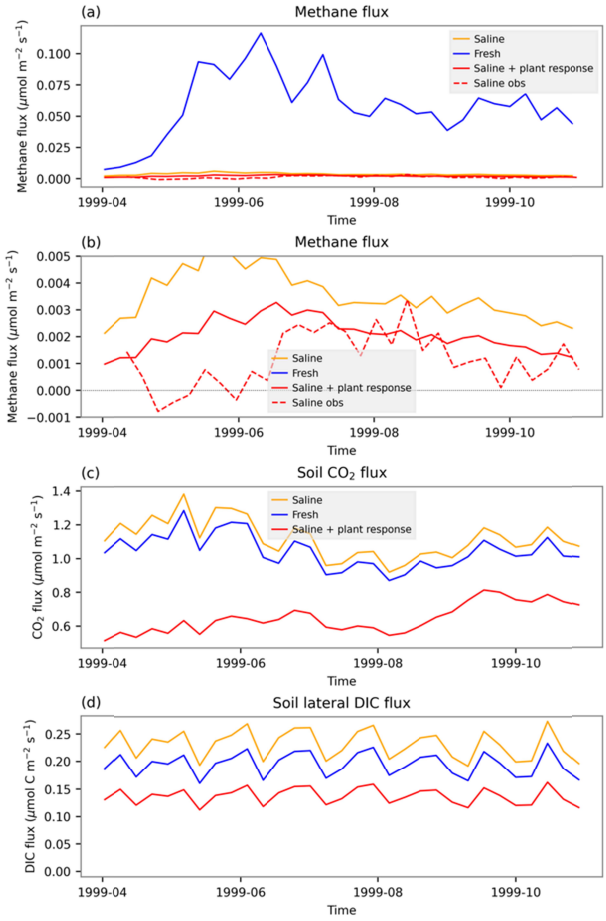

Figure 5: Simulated surface greenhouse gas fluxes over a two year period. (a): Methane fluxes. (b): Same as a, but magnifying the vertical axis so measured and simulated methane flux from the saline site are visible. (c): Soil CO_2 flux. Note that autotrophic respiration is excluded. (d): Lateral flux of DIC out of the soil column.

Soil organic carbon concentration profiles (Fig. 6) peaked at about 10 cm depth, reflecting more rapid decomposition in periodically unsaturated shallow layers and reduced inputs in deeper layers. C concentrations were slightly higher in the saline configuration compared to the fresh configuration, despite higher DIC production in the saline simulations. When salinity was combined with reduced GPP, soil carbon concentrations were about 50% lower. Observed SOC concentrations were generally lower than simulated SOC concentrations and did not decline as steeply with depth. Simulated SOC concentration approached the range of observations at 90-100 cm depth in the salinity + reduced GPP simulation.

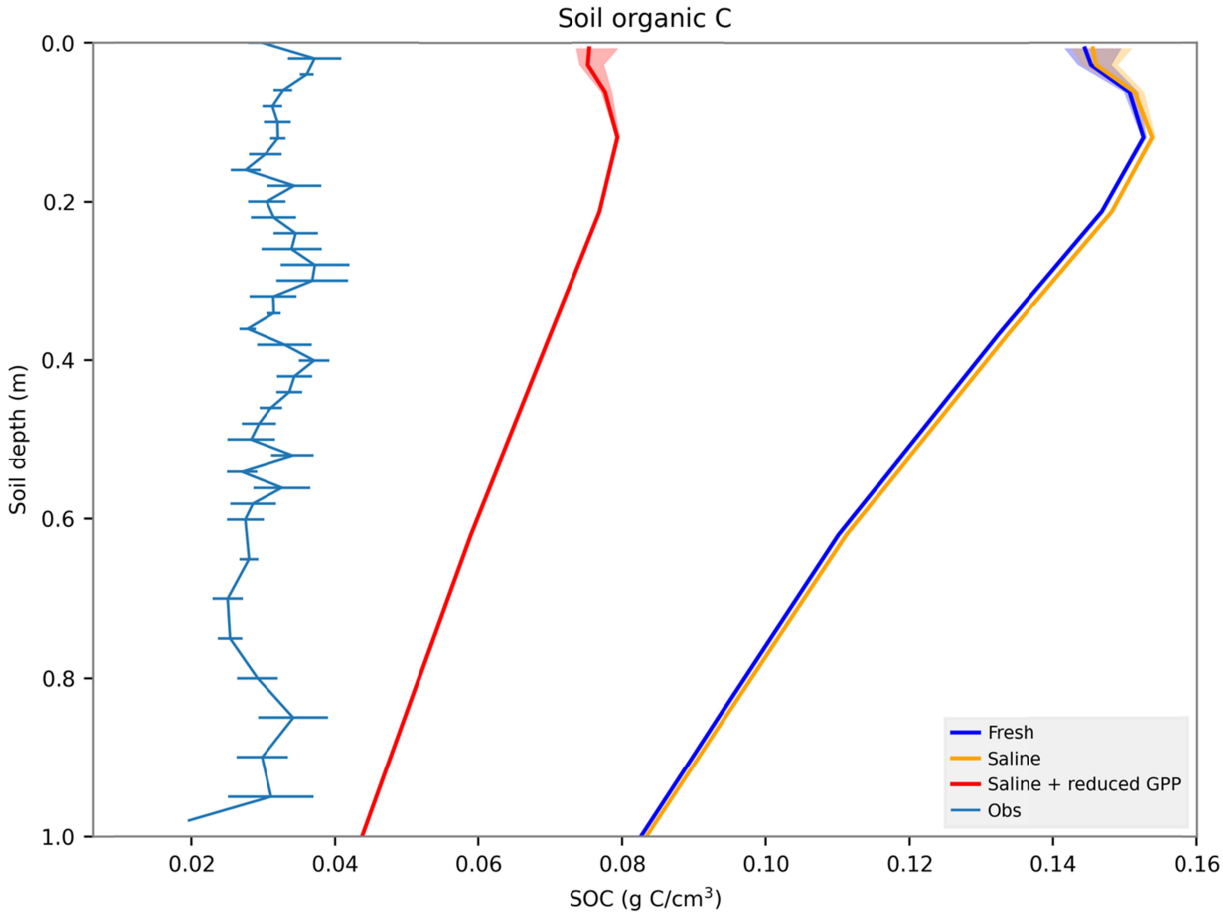

Figure 6: Profiles of simulated soil organic carbon concentrations for the three simulations. Line colors show the three simulations (Fresh, Saline, and Saline with reduced GPP). Shaded regions show the 10th to 90th percentile range of values over one year. Observed data from Spivak et al., 2020. Error bars show standard error across three replicate profiles.

In addition to carbon and sulfur, the reaction network also included iron redox cycling, allowing simulations of iron oxide and iron sulfide mineral precipitation and dissolution. Fe(II) concentrations were much higher in the freshwater than in the saline simulation, reflecting the rapid precipitation of Fe(II) into iron sulfide minerals in the more sulfidic saline simulation. Fe(II) concentrations in the fresh simulation peaked around 15-20 cm depth, reflecting the anoxic conditions and high DOC concentrations necessary to drive iron reduction. Iron oxide concentrations were high in the more oxic surface layers and lower in deeper layers. The fresh simulation showed net iron oxide loss to dissolution in anoxic layers, while the saline simulation had relatively slow rates of iron oxide accumulation in anoxic layers. Iron sulfide concentrations were higher in the saline than in the fresh simulation, and net iron sulfide precipitation rates were highest in shallower layers in the saline simulation, reflecting higher available iron.

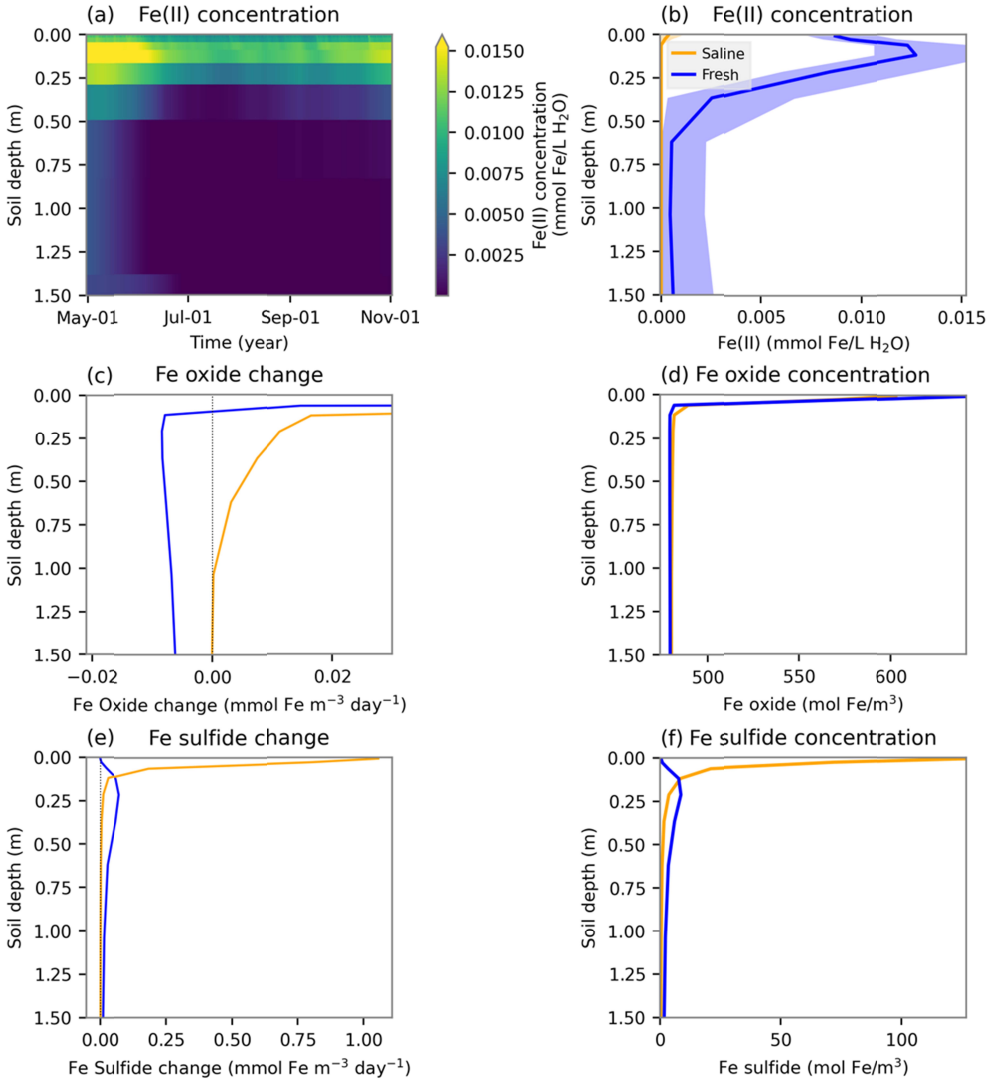

Figure 7: Simulated iron and iron sulfide cycling. (a): Fe(II) concentration as a function of depth and time in the freshwater simulation. (b): Mean profiles and 10-90 percentile of Fe(II) in fresh and saline simulations. (c): Mean rate of change of iron oxide mineral concentration. (d): Iron oxide mineral concentration profile. (e): Rate of change of iron sulfide mineral concentration. (f): Iron sulfide mineral concentration profile.

4 Discussion

4.1 Biogeochemical insights for modeling coastal wetlands

Our model framework successfully incorporated tidal-driven hydrology, redox biogeochemistry, and pH dynamics, into a full-featured LSM, allowing simulations of variations in subsurface biogeochemical cycling driven by rapid hydrological fluctuations in the context of carbon cycling. Model simulations connected higher sulfate concentrations in saline wetlands to lower DOC and higher DIC concentrations along with greatly reduced methane emissions. The higher fluxes from the freshwater simulation were consistent with (Sanders-DeMott et al., 2022), who

found that methane flux increased strongly along a saline to freshwater gradient in coastal wetlands, although our model simulated about half the magnitude of methane flux in freshwater end of the gradient compared to that study. The ability to simulate suppression of methane production under salinization is key to accurately predicting coastal wetland greenhouse gas balance (Kirwan et al., 2023).

Simulated SOC concentrations were slightly higher in the saline simulation than in the fresh simulation, despite the role of sulfate as a terminal electron acceptor. The difference is likely due to a slightly (2%) higher simulated GPP in the saline simulation compared to the fresh simulation, possibly driven by biogeochemical interactions with nutrient availability. When the impact of salinity on GPP was taken into account by reducing GPP, SOC concentrations were much lower. This result suggests that sulfate reduction alone may not be sufficient to explain differences in soil carbon patterns between saline and freshwater wetlands, and that plant-soil feedbacks may be necessary to explain contrasts. Plant feedbacks have been hypothesized to play a major role in peat collapse associated with salinization (Chambers et al., 2019). However, evidence that seawater additions can enhance SOC mineralization (Chambers et al., 2011)

4.2 Value of simulating detailed biogeochemical interactions in LSMs

While many existing LSMs, including the E3SM Land Model, do include methane production and emission calculations (Riley et al., 2011; Wania et al., 2013), our simulations highlight the potential importance of more complex interactions in determining decomposition and greenhouse gas production. Previous studies have identified substrate limitation as a driver of seasonal patterns in methane production (Chang et al., 2020). pH dynamics can also influence methane production, both by direct impacts on microbial physiology (Wagner et al., 2017) and by changing the solubility of alternative terminal electron acceptors such as iron (Marquart et al., 2019; B. N. Sulman et al., 2022). Here, we demonstrate the capability of simulating substrate dynamics, pH changes, oxygen depletion, and their influences on methane emissions within a full-featured land surface model. While we focus on methane production in this analysis, other important processes that this model framework can enable include the phytotoxic effect of sulfide in soils (Koch et al., 1990; Lamers et al., 2013), impacts of drought-driven increases in soil salinity concentration on vegetation and microbial communities, and interactions of pH dynamics with subsurface biogeochemistry. pH is widely considered a critical environmental variable, affecting carbon storage, microbiology, plant growth, and nutrient availability in environmental systems (Fierer & Jackson, 2006; Neina, 2019). Yet, dynamic pH is not included in current LSM frameworks. Thus, the ability to simulate dynamic pH in an LSM represents a significant step forward.

The incorporation of subsurface DIC concentrations and DIC loss in runoff is an important step forward toward representing the carbon balance of coastal wetland ecosystems, where lateral export of DIC and total alkalinity can be an important component of the net carbon balance, with total inorganic alkalinity export representing a long-term carbon sink in the ocean (Reithmaier et al., 2021; Yau et al., 2022). However, the current biogeochemical parameterization has not been evaluated in detail for the accuracy of DIC speciation (i.e., what fraction of DIC is in the form of bicarbonate versus carbonate and aqueous CO_2) and will need attention to other elemental cycles such as calcium to produce accurate estimates of total inorganic alkalinity production. In any case, the coupling of ELM to a detailed reaction network simulator provides the technical capability for incorporating total alkalinity production and balance into a land surface model.

While this paper focused on simulating redox dynamics, the reactive transport framework used in the model implementation builds the groundwork for a wide range of applications. PFLOTRAN includes a broad set of geochemical reaction capabilities, including microbially-mediated as well as abiotic aqueous reactions, dissolution and precipitation of different types of minerals, and sorption of solutes onto mineral surfaces (Steefel et al., 2015). The direct coupling of PFLOTRAN chemistry into ELM means that any geochemical reactions implemented in PFLOTRAN can be directly incorporated into land model simulations with minimal edits to land model code. Thus, this framework could be easily adapted to facilitate various applications including testing different decomposition reaction networks, simulating dynamics of inorganic carbon storage and release from carbonate minerals, and cycling of micronutrients within the soil. PFLOTRAN's Reaction Sandbox, which allows for customized geochemical formulations to be implemented in PFLOTRAN code (Hammond, 2022), opens broad possibilities for testing geochemistry and biogeochemical interactions within a coupled ELM-PFLOTRAN system. Furthermore, the implementation of the ELM coupling using the Alquimia API opens the possibility of coupling ELM other reactive transport codes that are compatible with the API and may have different reaction simulation capabilities.

4.3 Areas for improvement of model implementation

The current model lacks a full set of boundary conditions for solutes in tidal flows, which are currently limited to salinity, sulfate, and pH. A major limitation of this approach is lack of nutrient inputs from surface water, which could lead to underestimated vegetation productivity. The lack of full solute boundary conditions including major cation and anion concentrations also makes it difficult to accurately quantify pH, DIC, and DOC dynamics of the simulated wetland. Future applications of this model framework would benefit from developing a full set of solute boundary conditions in river and tidal waters.

The one-dimensional representation of subsurface hydrology in ELM posed challenges for directly integrating reactive transport into ELM. The ELM hydrology model was designed primarily for simulating grid cell water balance and water limitation of vegetation. Lateral flows, including subsurface drainage and tide-driven lateral flows, are not fully integrated into the hydrological solver. Rather, the model calculates vertical redistribution using a Richards equation approach and afterward adds or removes water associated with lateral flows using a filling/emptying bucket approach. This causes calculated lateral and vertical flows to be inconsistent with the full set of water flows, leading to unrealistic salinities due to flow convergence and high flow velocities within the column when using ELM-simulated water flow rates directly for reactive transport calculations. In the current study, we ultimately replaced the internally calculated vertical flow rates with approximate flows that were consistent with subsurface drainage. The lack of full solute boundary conditions could also have contributed to unrealistic results when using internally calculated flow rates. Further work in this area could benefit from fully integrating lateral flows into the ELM hydrological model and simulating lateral flows using hydraulic head boundary conditions rather than height differentials. As an intermediate step, 3-dimensional simulations of hydrologic flows in coastal wetland sediments could be used to inform the parameterization of column-scale hydrological exchanges in ELM.

The current lateral flow implementation imposes hydrological flows as boundary conditions on the ELM column and does not fully integrate hydrological exchanges or solute flows with other components of the E3SM, such as the river model (MOSART) and ocean model (MPAS-Ocean) (Golaz et al., 2019). Fully integrating coastal wetland processes into the Earth

system model will require coupling hydrological and solute exchanges across model components so that water, carbon, and other metrics can be conserved in large-scale simulations. The boundary condition approach used here builds the groundwork for incorporating these exchanges into the Earth system model coupler framework.

The implementation of gas transport in the soil column could also be improved. The current implementation includes moisture-dependent gas diffusion as well as a simple implementation of ebullition but does not include plant-mediated gas transport. Plant-mediated transport can be an important pathway for both methane transport out of the soil and oxygen transport into the soil, especially for aerenchymous plants (Colmer, 2003; Jeffrey et al., 2019; Noyce et al., 2023). Planned work on this model framework will include plant-mediated gas transport, with dependence on plant traits such as aerenchymous tissues and rooting depth distributions at the plant functional type level (LaFond-Hudson & Sulman, 2023). The implementation of ebullition also uses a simple approach that calculates partial pressure separately for each dissolved gas. This approach may underestimate ebullition flux when multiple dissolved gases are produced in the subsurface (e.g., methane, CO_2, and H_2S). An improved approach would incorporate gas mixing in bubbles, and we plan to move toward that approach in ongoing work. The current gas diffusion implementation does not explicitly divide soluble gases into dissolved and gas phases, but instead differentiates dissolved gases from non-gas solutes using diffusion coefficients. A two phase (gas and aqueous) transfer scheme that tracked the dissolved fraction of gases in each layer could lead to improved gas transport simulations.

Model parameterization is also a challenge, particularly for increasingly complex biogeochemical reaction networks. Our model parameterization does incorporate field and laboratory measurements of reaction rates and solute concentrations where possible (Table 1), but some parameters are inevitably difficult to constrain. In this initial study, we focused on demonstrating the feasibility of simulating reaction network interactions within a land surface model, and therefore did not evaluate modeled rates in detail. Applications of this framework to predictive modeling of biogeochemical cycling will benefit from additional detailed evaluation of reaction rates and concentrations in the context of porewater concentration and flux measurements. Additional parameterization of soil column hydraulic properties could also help to improve the accuracy of simulated hydrology, such as the overestimate of water table declines during low tide (Fig. 3a).

5 Conclusions

We coupled a biogeochemical reaction network solver (PFLOTRAN) to a land surface model (ELM) and implemented vertical solute and gas transport as well as tidal-driven inputs of salinity and sulfate. We applied the model to simulate biogeochemical cycling in Massachusetts tidal marshes under either saline or freshwater tidal boundary conditions. The coupled model framework allowed simulations of multiple redox reactions, pH dynamics, oxygen consumption, and methane production and oxidation to be fully integrated within a land surface model. Sulfate supplied in the saline simulation drove high levels of sulfate reduction, which reduced DOC, increased DIC, and greatly lowered subsurface methane concentrations and surface methane emissions. This new model framework builds the foundation for simulating multicomponent biogeochemical interactions in land surface models and demonstrates how directly simulating redox reactions in inundated soils can improve model simulations of organic matter decomposition and greenhouse gas production while building the groundwork for explicit

geochemical representation in larger-scale land surface model and Earth system model simulations.

Acknowledgements:
This work was supported by the U.S. Department of Energy Office of Science Early Career Research program as part of research in Earth System Model Development within the Earth and Environmental Systems Modeling Program. This research used resources of the Compute and Data Environment for Science (CADES) at the Oak Ridge National Laboratory, which is supported by the Office of Science of the U.S. Department of Energy under Contract No. DE-AC05-00OR22725. S.M. and G.H. acknowledge support from the IDEAS-Watersheds project, funded by the U.S. Department of Energy, Office of Science, Office of Biological and Environmental Research (Contract No DE-AC02-05CH11231), for the development of Alquimia and PFLOTRAN. Salary support to AEG came from OCE 2224608. PNNL is operated for the DOE by Battelle Memorial Institute under contract DE-AC05-76RL01830.

Data availability:
Model code, forcing, and output data are available through the ESS-Dive data repository: https://data.ess-dive.lbl.gov/datasets/doi:10.15485/1991625 (B. N. Sulman et al., 2023)
Porewater concentration data are available through the LTER data repository: https://doi.org/10.6073/pasta/1099aefc63208d9405df293667f6a83d
Eddy covariance data are available through the LTER data repository: https://doi.org/10.6073/pasta/a1fff894a469042bceeff05561a3d9f7
Water level data are available through the LTER data repository: https://doi.org/10.6073/PASTA/605232AED464701C5B576C54F1CA7F62
Soil profile data are available from (Spivak, 2020) https://doi.org/10.26008/1912/bco-dmo.827298.1

Andre, B., Molins, S., Johnson, J., & Steefel, C. (2013). *Alquimia*. Lawrence Berkeley National Laboratory (LBNL), Berkeley, CA (United States). https://doi.org/10.11578/DC.20210416.49

Breteler, R. J., Teal, J. M., Giblin, A. E., & Valiela, I. (1981). Trace element enrichments in decomposing litter of Spartina alterniflora. *Aquatic Botany*, *11*, 111–120.

Burrows, S. M., Maltrud, M., Yang, X., Zhu, Q., Jeffery, N., Shi, X., et al. (2020). The DOE E3SM v1.1 Biogeochemistry Configuration: Description and Simulated Ecosystem-Climate Responses to Historical Changes in Forcing. *Journal of Advances in Modeling Earth Systems*, *12*(9). https://doi.org/10.1029/2019MS001766

Carrayrou, J., Mosé, R., & Behra, P. (2004). Operator-splitting procedures for reactive transport and comparison of mass balance errors. *Journal of Contaminant Hydrology*, *68*(3–4), 239–268.

Chambers, L. G., Reddy, K. R., & Osborne, T. Z. (2011). Short-term response of carbon cycling to salinity pulses in a freshwater wetland. *Soil Science Society of America Journal. Soil Science Society of America*, *75*(5), 2000–2007.

Chambers, L. G., Steinmuller, H. E., & Breithaupt, J. L. (2019). Toward a mechanistic understanding of "peat collapse" and its potential contribution to coastal wetland loss. *Ecology*, *100*(7), e02720.

Chang, K.-Y., Riley, W. J., Crill, P. M., Grant, R. F., & Saleska, S. R. (2020). Hysteretic temperature sensitivity of wetland CH_4 fluxes explained by substrate availability and microbial activity. *Biogeosciences* , *17*(22), 5849–5860.

Colmer, T. D. (2003). Long-distance transport of gases in plants: a perspective on internal aeration and radial oxygen loss from roots. *Plant, Cell & Environment*, *26*(1), 17–36.

Estop-Aragonés, C., Knorr, K. H., & Blodau, C. (2013). Belowground in situ redox dynamics and methanogenesis recovery in a degraded fen during dry-wet cycles and flooding. *Biogeosciences* , *10*(1), 421–436.

Fan, Z., Neff, J. C., Waldrop, M. P., Ballantyne, A. P., & Turetsky, M. R. (2014). Transport of oxygen in soil pore-water systems: implications for modeling emissions of carbon dioxide and methane from peatlands. *Biogeochemistry*, *121*(3), 455–470.

Fierer, N., & Jackson, R. B. (2006). The diversity and biogeography of soil bacterial communities. *Proceedings of the National Academy of Sciences of the United States of America*, *103*(3), 626–631.

Frei, S., Knorr, K. H., Peiffer, S., & Fleckenstein, J. H. (2012). Surface micro-topography causes hot spots of biogeochemical activity in wetland systems: A virtual modeling experiment. *Journal of Geophysical Research*, *117*, 18.

Giblin, A. (2021). Marsh water table height, logging data from the Shad Creek Spartina marsh site for April-November 2019, Rowley, MA, PIE LTER [Data set]. Environmental Data Initiative. https://doi.org/10.6073/PASTA/605232AED464701C5B576C54F1CA7F62

Giblin, A., & Forbrich, I. (2022). Eddy flux measurements during 2015 from low marsh site (Spartina alterniflora) within Shad Creek catchment, Rowley, Massachusetts [Data set]. Environmental Data Initiative. https://doi.org/10.6073/PASTA/A1FFF894A469042BCEEFF05561A3D9F7

Giblin, A., Hopkinson, C., & Lter, P. I. E. (2021). PIE LTER marsh sediment porewater nutrient concentrations from Spartina sp. and Typha sp. sites along the Parker River and Rowley River, MA [Data set]. Environmental Data Initiative. https://doi.org/10.6073/PASTA/1099AEFC63208D9405DF293667F6A83D

Ginn, B., Meile, C., Wilmoth, J., Tang, Y., & Thompson, A. (2017). Rapid Iron Reduction Rates Are Stimulated by High-Amplitude Redox Fluctuations in a Tropical Forest Soil. *Environmental Science & Technology*, *51*(6), 3250–3259.

Golaz, J., Caldwell, P. M., Van Roekel, L. P., Petersen, M. R., Tang, Q., Wolfe, J. D., et al. (2019). The DOE E3SM Coupled Model Version 1: Overview and Evaluation at Standard Resolution. *Journal of Advances in Modeling Earth Systems*, *11*(7), 2089–2129.

Hall, S. J., Berhe, A. A., & Thompson, A. (2018). Order from disorder: do soil organic matter composition and turnover co-vary with iron phase crystallinity? *Biogeochemistry*, *140*(1), 93–110.

Hammond, G. E. (2022). The PFLOTRAN Reaction Sandbox. *Geoscientific Model Development*, *15*(4), 1659–1676.

Hammond, G. E., Lichtner, P. C., & Mills, R. T. (2014). Evaluating the performance of parallel subsurface simulators: An illustrative example with PFLOTRAN. *Water Resources Research*, *50*(1), 208–228.

Herndon, E. M., Mann, B. F., Roy Chowdhury, T., Yang, Z., Wullschleger, S. D., Graham, D., et al. (2015). Pathways of anaerobic organic matter decomposition in tundra soils from Barrow, Alaska. *Journal of Geophysical Research G: Biogeosciences*, *120*(11), 2345–2359.

Inglett, K. S., Inglett, P. W., Reddy, K. R., & Osborne, T. Z. (2012). Temperature sensitivity of greenhouse gas production in wetland soils of different vegetation. *Biogeochemistry*, *108*(1), 77–90.

Iversen, N., & Jorgensen, B. B. (1985). Anaerobic methane oxidation rates at the sulfate-methane transition in marine sediments from Kattegat and Skagerrak (Denmark). *Limnology and Oceanography*, *30*(5), 944–955.

Jan, A., Coon, E. T., & Painter, S. L. (2021). Toward more mechanistic representations of biogeochemical processes in river networks: Implementation and demonstration of a multiscale model. *Environmental Modelling & Software*, *145*, 105166.

Jeffrey, L. C., Maher, D. T., Johnston, S. G., Kelaher, B. P., Steven, A., & Tait, D. R. (2019). Wetland methane emissions dominated by plant-mediated fluxes: Contrasting emissions pathways and seasons within a shallow freshwater subtropical wetland. *Limnology and Oceanography*, *64*(5), 1895–1912.

King, G. M., Roslev, P., & Skovgaard, H. (1990). Distribution and rate of methane oxidation in sediments of the Florida everglades. *Applied and Environmental Microbiology*, *56*(9), 2902–2911.

Kirwan, M. L., Megonigal, J. P., Noyce, G. L., & Smith, A. J. (2023). Geomorphic and ecological constraints on the coastal carbon sink. *Nature Reviews. Earth & Environment*, *4*(6), 393–406.

Koch, M. S., Mendelssohn, I. A., & McKee, K. L. (1990). Mechanism for the hydrogen sulfide-induced growth limitation in wetland macrophytes. *Limnology and Oceanography*, *35*(2), 399–408.

Kögel-Knabner, I., Amelung, W., Cao, Z., Fiedler, S., Frenzel, P., Jahn, R., et al. (2010). Biogeochemistry of paddy soils. *Geoderma*, *157*(1), 1–14.

Koven, C. D., Riley, W. J., Subin, Z. M., Tang, J. Y., Torn, M. S., Collins, W. D., et al. (2013). The effect of vertically resolved soil biogeochemistry and alternate soil C and N models on C dynamics of CLM4. *Biogeosciences* , *10*(11), 7109–7131.

LaFond-Hudson, S., & Sulman, B. (2023). Modeling strategies and data needs for representing coastal wetland vegetation in land surface models. *The New Phytologist*, *238*(3), 938–951.

Lamers, L., Govers, L., Janssen, I., Geurts, J., Van der Welle, M., Van Katwijk, M., et al. (2013). Sulfide as a soil phytotoxin—a review. *Frontiers in Plant Science*, *4*. https://doi.org/10.3389/fpls.2013.00268

Li, H., Santos, F., Butler, K., & Herndon, E. (2021). A critical review on the multiple roles of manganese in stabilizing and destabilizing soil organic matter. *Environmental Science & Technology*, (acs.est.1c00299). https://doi.org/10.1021/acs.est.1c00299

822 Lipson, D. A., Jha, M., Raab, T. K., & Oechel, W. C. (2010). Reduction of iron (III) and humic
823 substances plays a major role in anaerobic respiration in an Arctic peat soil. *Journal of*
824 *Geophysical Research: Biogeosciences*, *115*(4), 1–13.
825 Marquart, K. A., Haller, B. R., Paper, J. M., Flynn, T. M., Boyanov, M. I., Shodunke, G., et al.
826 (2019). Influence of pH on the balance between methanogenesis and iron reduction.
827 *Geobiology*, *17*(2), 185–198.
828 McLeod, E., Chmura, G. L., Bouillon, S., Salm, R., Björk, M., Duarte, C. M., et al. (2011). A
829 blueprint for blue carbon: Toward an improved understanding of the role of vegetated
830 coastal habitats in sequestering CO2. *Frontiers in Ecology and the Environment*, *9*(10),
831 552–560.
832 Molins, S., Svyatsky, D., Xu, Z., Coon, E. T., & Moulton, J. D. (2022). A multicomponent
833 reactive transport model for integrated surface-subsurface hydrology problems. *Water*
834 *Resources Research*, *58*(8). https://doi.org/10.1029/2022wr032074
835 Neina, D. (2019). The Role of Soil pH in Plant Nutrition and Soil Remediation. *Applied and*
836 *Environmental Soil Science*, *2019*. https://doi.org/10.1155/2019/5794869
837 Noyce, G. L., Smith, A. J., Kirwan, M. L., Rich, R. L., & Megonigal, J. P. (2023). Oxygen
838 priming induced by elevated CO2 reduces carbon accumulation and methane emissions
839 in coastal wetlands. *Nature Geoscience*, *16*(1), 63–68.
840 O'Meara, T. A., Thornton, P. E., Ricciuto, D. M., Noyce, G. L., Rich, R. L., & Megonigal, J. P.
841 (2021). Considering coasts: Adapting terrestrial models to characterize coastal wetland
842 ecosystems. *Ecological Modelling*, *450*, 109561.
843 Patankar, S. V. (1980). *Numerical Heat Transfer and Fluid Flow*. Taylor & Francis.

844 Peng, Y., Fornara, D. A., Wu, Q., Heděnec, P., Yuan, J., Yuan, C., et al. (2023). Global patterns
845 and driving factors of plant litter iron, manganese, zinc, and copper concentrations. *The*
846 *Science of the Total Environment*, *857*(Pt 3), 159686.
847 Perzan, Z., Babey, T., Caers, J., Bargar, J. R., & Maher, K. (2021). Local and global sensitivity
848 analysis of a reactive transport model simulating floodplain redox cycling. *Water*
849 *Resources Research*, *57*(12). https://doi.org/10.1029/2021wr029723
850 Poffenbarger, H. J., Needelman, B. A., & Megonigal, J. P. (2011). Salinity influence on methane
851 emissions from tidal marshes. *Wetlands*, *31*(5), 831–842.
852 Reithmaier, G. M. S., Johnston, S. G., Junginger, T., Goddard, M. M., Sanders, C. J., Hutley, L.
853 B., et al. (2021). Alkalinity production coupled to pyrite formation represents an
854 unaccounted blue carbon sink. *Global Biogeochemical Cycles*, *35*(4).
855 https://doi.org/10.1029/2020gb006785
856 Riley, W. J., Subin, Z. M., Lawrence, D. M., Swenson, S. C., Torn, M. S., Meng, L., et al.
857 (2011). Barriers to predicting changes in global terrestrial methane fluxes: analyses using
858 CLM4Me, a methane biogeochemistry model integrated in CESM. *Biogeosciences* , *8*(7),
859 1925–1953.
860 Sanders-DeMott, R., Eagle, M. J., Kroeger, K. D., Wang, F., Brooks, T. W., O'Keefe Suttles, J.
861 A., et al. (2022). Impoundment increases methane emissions in Phragmites-invaded
862 coastal wetlands. *Global Change Biology*, *28*(15), 4539–4557.
863 Shi, X., Thornton, P. E., Ricciuto, D. M., Hanson, P. J., Mao, J., Sebestyen, S. D., et al. (2015).
864 Representing northern peatland microtopography and hydrology within the Community
865 Land Model. *Biogeosciences* , *12*(21), 6463–6477.

Sollins, P., Homann, P., & Caldwell, B. A. (1996). Stabilization and destabilization of soil organic matter: Mechanisms and controls. *Geoderma*, *74*, 65–105.

Spivak, A. (2020). Bulk soil and elemental properties of marsh and infilled pond soils collected in 2014-2015 within Plum Island Ecosystems LTER [Data set]. Biological and Chemical Oceanography Data Management Office (BCO-DMO). https://doi.org/10.26008/1912/BCO-DMO.827298.1

Steefel, C. I., Appelo, C. A. J., Arora, B., Jacques, D., Kalbacher, T., Kolditz, O., et al. (2015). Reactive transport codes for subsurface environmental simulation. *Computational Geosciences*, *19*(3), 445–478.

Strang, G. (1968). On the Construction and Comparison of Difference Schemes. *SIAM Journal on Numerical Analysis*, *5*(3), 506–517.

Sulman, B. N., Yuan, F., O'Meara, T., Gu, B., Herndon, E. M., Zheng, J., et al. (2022). Simulated hydrological dynamics and coupled iron redox cycling impact methane production in an arctic soil. *Journal of Geophysical Research. Biogeosciences*, *127*(10). https://doi.org/10.1029/2021jg006662

Sulman, B. N., Wang, J., LaFond-Hudson, S., O'Meara, T., Yuan, F., Molins, S., et al. (2023). Model simulations of Plum Island Ecosystems LTER low marsh site using ELM-PFLOTRAN [Data set]. Environmental System Science Data Infrastructure for a Virtual Ecosystem; Simulating estuarine wetland function: Nitrogen removal, carbon sequestration, and greenhouse gas fluxes at the river-land-ocean interface. https://doi.org/10.15485/1991625

887 Sutton-Grier, A. E., Keller, J. K., Koch, R., Gilmour, C., & Megonigal, J. P. (2011). Electron
888 donors and acceptors influence anaerobic soil organic matter mineralization in tidal
889 marshes. *Soil Biology & Biochemistry*, *43*(7), 1576–1583.
890 Tang, G., Yuan, F., Bisht, G., Hammond, G. E., Lichtner, P. C., Kumar, J., et al. (2016).
891 Addressing numerical challenges in introducing a reactive transport code into a land
892 surface model: A biogeochemical modeling proof-of-concept with CLM-PFLOTRAN
893 1.0. *Geoscientific Model Development*, *9*(3), 927–946.
894 Tang, J., Riley, W. J., & Zhu, Q. (2022). Supporting hierarchical soil biogeochemical modeling:
895 version 2 of the Biogeochemical Transport and Reaction model (BeTR-v2). *Geoscientific*
896 *Model Development*, *15*(4), 1619–1632.
897 Thornton, P. E., & Rosenbloom, N. A. (2005). Ecosystem model spin-up: Estimating steady state
898 conditions in a coupled terrestrial carbon and nitrogen cycle model. *Ecological*
899 *Modelling*, *189*(1–2), 25–48.
900 Thornton, P. E., Law, B. E., Gholz, H. L., Clark, K. L., Falge, E., Ellsworth, D. S., et al. (2002).
901 Modeling and measuring the effects of disturbance history and climate on carbon and
902 water budgets in evergreen needleleaf forests. *Agricultural and Forest Meteorology*,
903 *113*(1), 185–222.
904 Todd-Brown, K. E. O., Randerson, J. T., Post, W. M., Hoffman, F. M., Tarnocai, C., Schuur, E.
905 A. G., & Allison, S. D. (2013). Causes of variation in soil carbon simulations from
906 CMIP5 Earth system models and comparison with observations. *Biogeosciences* , *10*(3),
907 1717–1736.
908 Vasquez, E. A., Glenn, E. P., Guntenspergen, G. R., Brown, J. J., & Nelson, S. G. (2006). Salt
909 tolerance and osmotic adjustment of Spartina alterniflora (Poaceae) and the invasive M

haplotype of Phragmites australis (Poaceae) along a salinity gradient. *American Journal of Botany*, *93*(12), 1784–1790.

Wagner, R., Zona, D., Oechel, W., & Lipson, D. (2017). Microbial community structure and soil pH correspond to methane production in Arctic Alaska soils. *Environmental Microbiology*, *19*(8), 3398–3410.

Wania, R., Melton, J. R., Hodson, E. L., Poulter, B., Ringeval, B., Spahni, R., et al. (2013). Present state of global wetland extent and wetland methane modelling: Methodology of a model inter-comparison project (WETCHIMP). *Geoscientific Model Development*, *6*(3), 617–641.

Ward, N. D., Megonigal, J. P., Bond-Lamberty, B., Bailey, V. L., Butman, D., Canuel, E. A., et al. (2020). Representing the function and sensitivity of coastal interfaces in Earth system models. *Nature Communications*, *11*(1), 2458.

Wright, J. V. (1990). *Diffusion coefficients and hydraulic conductivity in unsaturated Hanford soils and sediments*. Pacific Northwest Lab., Richland, WA (USA).

Xu, Z., Molins, S., Özgen-Xian, I., Dwivedi, D., Svyatsky, D., Moulton, J. D., & Steefel, C. (2022). Understanding the hydrogeochemical response of a mountainous watershed using integrated surface-subsurface flow and reactive transport modeling. *Water Resources Research*, *58*(8). https://doi.org/10.1029/2022wr032075

Yang, X., Thornton, P. E., Ricciuto, D. M., & Post, W. M. (2014). The role of phosphorus dynamics in tropical forests - A modeling study using CLM-CNP. *Biogeosciences* , *11*(6), 1667–1681.

931 Yau, Y. Y. Y., Xin, P., Chen, X., Zhan, L., Call, M., Conrad, S. R., et al. (2022). Alkalinity
932 export to the ocean is a major carbon sequestration mechanism in a macrotidal saltmarsh.
933 *Limnology and Oceanography*. https://doi.org/10.1002/lno.12155